hydrogen

MDPI

Article

Hydrogen Isotope Permeation, Retention, and Embrittlement Response of 310S Austenitic Stainless Steel Under High-Temperature Gaseous Deuterium Charging

Yulong Jiang, Zhifu Wang, Jian Li and Zhonghao Heng *

School of Mechanical Engineering, Qinghai University, Xining 810016, China; jiangyulong@qhu.edu.cn (Y.J.); wangzhifu@qhu.edu.cn (Z.W.); lijian1979@qhu.edu.cn (J.L.)
* Correspondence: hengzhonghao@qhu.edu.cn

Abstract

High-temperature gaseous deuterium charging was used to investigate hydrogen isotope permeation, retention, microstructural stability, and fracture response in 310S austenitic stainless steel. Gas-driven permeation, thermal desorption spectroscopy, two-dimensional diffusion simulation, XRD/EBSD characterization, tensile testing, and fractographic analysis were combined to correlate isotope transport with mechanical and fracture behavior. The deuterium permeability and diffusion coefficient followed an Arrhenius relationship, and the diffusion coefficient extrapolated at 673 K was 1.11×10^{-11} m^2/s. With increasing charging time, the deuterium distribution evolved from a surface-enriched unsaturated state to an overall near-saturated state with higher retention. Although deuterium charging had little influence on yield strength, ultimate tensile strength, and elongation under the present room-temperature tensile condition, local quasi-cleavage-like facets, secondary cracks, and serrated fracture edges became more evident after charging. These results indicate that the embrittlement response of 310S stainless steel was mainly characterized by localized hydrogen-assisted damage rather than dominant brittle fracture.

Keywords: high-temperature gaseous deuterium charging; hydrogen isotopes; permeation and retention; hydrogen embrittlement

1. Introduction

Hydrogen embrittlement (HE) is a critical issue compromising the structural reliability of metallic materials in hydrogen production, storage, and transportation systems. Upon ingress into metals, hydrogen degrades ductility and load-bearing capacity, promotes crack initiation and propagation, and eventually leads to premature brittle failure. Consequently, the compatibility of structural materials with hydrogen environments is paramount for the safety of hydrogen-related infrastructure [1–5].

Among candidate materials, austenitic stainless steels are widely considered promising for hydrogen service due to their face-centered cubic (FCC) structure, relatively high hydrogen solubility, low diffusivity, and an excellent balance of toughness, corrosion resistance, and processability [6–8]. In particular, 310S stainless steel, characterized by high Cr and Ni contents and superior thermal stability, has demonstrated significant potential for hydrogen-containing equipment [9,10]. Nevertheless, even stable austenitic stainless steels may undergo hydrogen-assisted plastic damage and fracture mode transitions under high-pressure or high-temperature hydrogen environments. Therefore, their hydrogen permeation, retention, and embrittlement mechanisms remain to be fully elucidated.

Academic Editor: Rui C. Vilão

Received: 13 April 2026
Revised: 5 May 2026
Accepted: 9 May 2026
Published: 12 May 2026

Previous studies have established that hydrogen transport in metals is generally governed by Fickian diffusion and can be strongly influenced by trapping at microstructural defects such as dislocations, grain boundaries, vacancies, twin boundaries, and phase or second-phase interfaces [2,11]. These defects not only affect the effective diffusion coefficient and the concentration of mobile hydrogen, but also determine local hydrogen enrichment and potential crack initiation sites. Hydrogen embrittlement is generally associated with multiple interacting mechanisms, including hydrogen-enhanced localized plasticity (HELP), hydrogen-enhanced decohesion (HEDE), and hydrogen-enhanced vacancy or defect accumulation [12–16]. The relative contribution of these mechanisms depends on hydrogen content and distribution, stress state, and microstructural parameters such as austenite stability, grain boundary character, dislocation density, twin boundaries, and second phases. For stable austenitic stainless steels, the FCC matrix and high austenite stability help suppress hydrogen-induced martensitic transformation and severe macroscopic embrittlement. Nevertheless, hydrogen can still accumulate in near-surface regions and defect-sensitive zones, leading to localized hydrogen-assisted damage and changes in fracture characteristics even when the overall tensile properties remain relatively stable.

Currently, electrochemical hydrogen charging remains the most prevalent experimental approach for evaluating HE susceptibility in austenitic steels [17]. Although convenient, this method possesses inherent limitations for stable austenitic grades. Due to their extremely low hydrogen diffusivity at room temperature, electrochemical charging typically results in high hydrogen concentrations confined to the near-surface region; achieving sufficient through-thickness diffusion requires prohibitively long charging times [9,18–22]. Moreover, the hydrogen distribution produced by electrochemical charging may deviate from that encountered in practical gaseous environments, and hydrogen loss during specimen transfer can further compromise the reliability of mechanical assessments [23,24].

By comparison, high-temperature gaseous hydrogen charging provides a more continuous and realistic hydrogen input, making it more suitable for investigating transport and retention under operational conditions. Furthermore, employing deuterium as a tracer isotope minimizes background hydrogen interference. Combined with gas-driven permeation (GDP) and thermal desorption spectroscopy (TDS), deuterium charging enables the quantitative evaluation of hydrogen isotope permeation, diffusion, trapping, and retention behavior [25–27]. When integrated with mechanical testing and fractographic analysis, this approach offers an effective route to correlate isotope distribution with damage evolution.

Although hydrogen behavior and embrittlement in austenitic stainless steels have been widely investigated, the coupled relationship among high-temperature gaseous deuterium permeation, retention, diffusion-state evolution, microstructural stability, and local fracture response in 310S stainless steel remains insufficiently clarified. In particular, it is still necessary to understand how different deuterium charging durations produce distinct isotope distribution states and how these states affect local fracture characteristics when the macroscopic tensile properties remain nearly unchanged. Therefore, the scientific novelty of this study lies in establishing the relationship between hydrogen isotope distribution and local damage evolution in 310S stainless steel by combining GDP-derived transport parameters, TDS-measured retention behavior, two-dimensional diffusion simulation, phase stability characterization, tensile testing, and fractographic analysis under high-temperature gaseous deuterium charging.

In this work, the hydrogen isotope permeation, retention, and embrittlement response of 310S austenitic stainless steel were investigated via high-temperature gaseous deuterium charging. Deuterium permeability and diffusion parameters were determined by GDP, and the retention behavior under different charging durations was characterized by TDS. The cross-sectional isotope distribution was evaluated using two-dimensional diffusion

simulation based on Fick's second law. In addition, XRD, EBSD, tensile testing, and SEM fractographic analysis were used to assess the microstructural stability, mechanical response, and fracture characteristics after deuterium charging. This study provides experimental insight into the localized hydrogen-assisted damage response of stable 310S stainless steel under high-temperature gaseous charging conditions.

2. Materials and Methods

2.1. Material and Heat Treatment

The experimental material was a commercial 310S austenitic stainless steel bar. Its chemical composition is listed in Table 1. All specimens used in this study were machined from the center region of the bar's thickness, with the sampling direction parallel to the rolling direction, in order to ensure microstructural consistency.

Table 1. Measured chemical composition of 310S austenitic stainless steel (wt.%).

	Cr	C	Mn	Ni	N	Mo	Nb	Si	Co	Ti
310S	24.03	0.04	1.05	19.01	0.06	0.31	0.02	0.37	0.2	0.004

The solution treatment process is shown in Figure 1. The specimens were solution treated at 1273 K for 120 min and then water quenched to room temperature before deuterium charging and subsequent characterization.

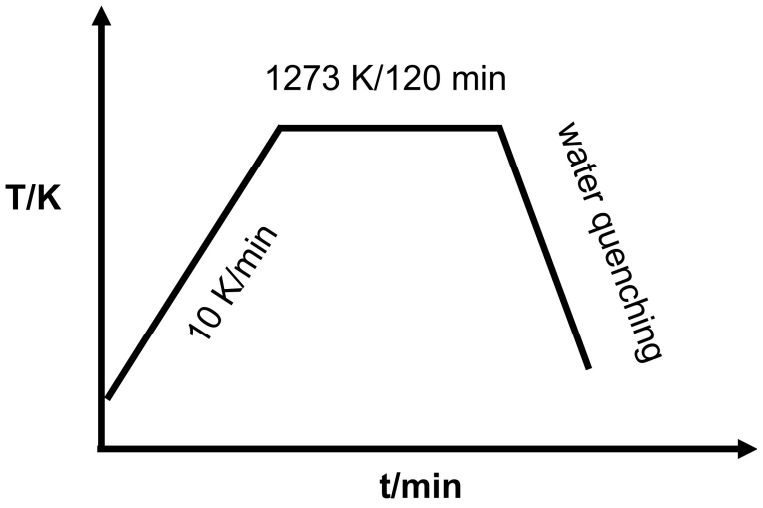

Figure 1. Schematic diagram of heat treatment process.

2.2. High-Temperature Gaseous Deuterium Charging and Hydrogen-Related Characterization

To reduce the interference of background hydrogen, deuterium gas was used as a stable hydrogen isotope tracer in the high-temperature gaseous charging experiments. Deuterium is commonly used to characterize hydrogen isotope transport and retention in metals because it has similar lattice occupation, trapping characteristics, and retention behavior to hydrogen, while its $m/z = 4$ signal can be distinguished from the background hydrogen signal during TDS and permeation measurements. Previous studies on austenitic stainless steels and fusion-relevant structural materials have shown that hydrogen isotopes are suitable for evaluating permeability, diffusivity, trapping, and retention behavior, and that deuterium charging combined with GDP and TDS is an effective approach for characterizing hydrogen isotope transport and retention [25–31]. However, since an isotope effect still exists between hydrogen and deuterium, the term "deuterium" is used in this paper when describing specific experimental procedures and measured parameters,

whereas the term "hydrogen" is used when discussing general mechanisms and material responses.

A gas-driven permeation platform was employed for gaseous deuterium charging of 310S stainless steel. Two types of specimens were prepared: small dog-bone tensile specimens for post-charging tensile testing and TDS, and disk specimens for GDP measurements. Prior to testing, all specimens were ground stepwise using SiC papers from 120 to 5000 grit, followed by electrolytic polishing in a solution containing 5 mL perchloric acid and 45 mL absolute ethanol. The polishing parameters were 18 V for 40 s. The specimens were then ultrasonically cleaned in absolute ethanol and sealed for storage to ensure a consistent surface condition.

Deuterium charging was carried out at 673 K. The charging temperature of 673 K was selected by considering both engineering relevance and experimental feasibility. In solid-state hydrogen storage systems, candidate structural materials for vessels and related components may be exposed to high-temperature hydrogen-containing environments during hydrogen absorption/desorption of metal hydride media. Mg-based metal hydrides and related high-temperature hydrogen storage materials generally operate or release hydrogen at elevated temperatures, typically within or near the range of 573–673 K [32,33]. Therefore, gaseous deuterium charging at 673 K provides a relevant high-temperature hydrogen-containing condition for evaluating hydrogen isotope ingress in 310S stainless steel. In addition, based on the diffusion coefficient extrapolated from the GDP results, this temperature allows for measurable deuterium ingress into millimeter-scale tensile specimens within several hours, while still distinguishing short-time surface-enriched charging from long-time near-saturated charging. To investigate the effect of charging time on the hydrogen-related behavior and mechanical response of 310S stainless steel, two charging durations, 1 min and 4 h, were selected. The corresponding specimens were denoted as 673 K-1 min-D and 673 K-4 h-D, respectively, while the solution-treated specimen without deuterium charging was denoted as RT. A combined GDP–TDS platform was used to evaluate the gaseous permeation and desorption behavior of hydrogen isotopes. During the permeation tests, Swagelok VCR fittings were used for specimen clamping and system sealing to ensure effective isolation and good gas tightness of the upstream and downstream chambers.

After deuterium charging, the desorption behavior of hydrogen isotopes was analyzed by TDS using the tensile specimens. The tests were conducted under a high-purity He atmosphere from room temperature to 1373 K at a heating rate of 10 K/min. The signal at m/z = 4 was continuously collected by a quadrupole mass spectrometer to obtain the deuterium desorption flux–temperature curves. The deuterium uptake per unit area was quantitatively determined by integrating the TDS curves, and the retention behavior under different charging durations was analyzed in combination with the desorption peak characteristics.

2.3. Microstructural Characterization

Phase analysis was carried out using a Bruker X-ray diffractometer made by Bruker, Billerica, MA, USA. The specimen size was 10 mm × 1.5 mm × 1.5 mm, and the scanned surface was parallel to the rolling direction. The scanning range was 20–100° in 2θ, with a scanning rate of 4°/min, an accelerating voltage of 40 kV, and a current of 150 mA.

The microstructure of the solution-treated specimen was characterized by optical microscopy. In addition, a field-emission scanning electron microscope equipped with an EBSD system (FE-SEM, Sigma-300, Carl Zeiss, Shanghai, China) was used to analyze the phase constitution and microstructural features of the specimens before and after deuterium charging. The EBSD step size was set to approximately 1/20 of the grain size. Fracture

morphologies of the tensile specimens under different conditions were also examined by scanning electron microscopy to analyze the changes in fracture characteristics after deuterium charging.

2.4. Tensile Testing

Plate-shaped miniature dog-bone tensile specimens were cut from the center region of the solution-treated bar thickness along the rolling direction, and their dimensions are shown in Figure 2. Tensile tests were conducted on an Instron 5848 universal testing machine at room temperature with an initial strain rate of 5×10^{-3} s^{-1} for the RT, 673 K-1 min-D, and 673 K-4 h-D conditions. The yield strength, ultimate tensile strength, and elongation after fracture were obtained from the engineering stress–strain curves. Unless otherwise stated, engineering stress and engineering strain are used throughout this work, and the yield strength was determined using the 0.2% offset method.

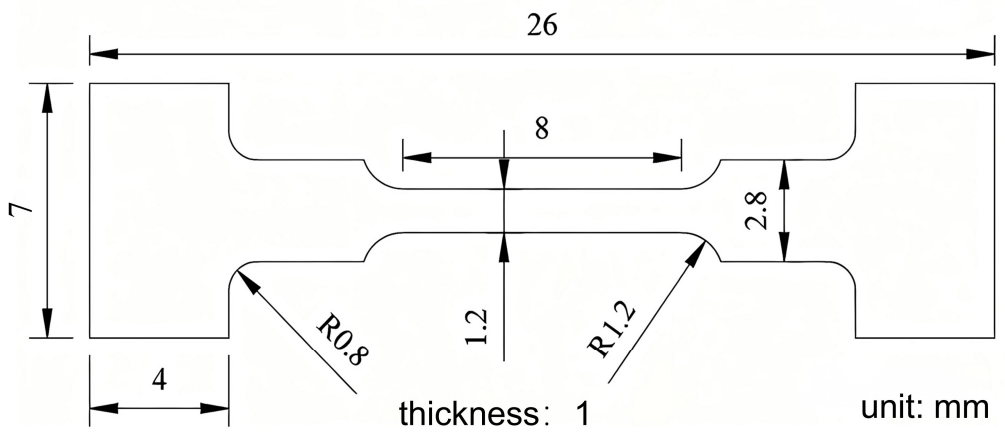

Figure 2. Dimensional schematic diagram of tensile specimen.

The hydrogen embrittlement sensitivity was evaluated by comparing the elongation after fracture before and after deuterium charging. The elongation loss was calculated as follows:

$$I_\delta = \frac{\delta_{RT} - \delta_D}{\delta_{RT}} \times 100\% \quad (1)$$

where I_δ is the elongation loss; δ_{RT} is the elongation after fracture of the uncharged specimen; and δ_D is the elongation after fracture of the deuterium-charged specimen. At least three repeated tests were conducted for each condition to ensure the reproducibility and reliability of the results.

3. Results

3.1. Gaseous Permeation and Diffusion Behavior at Different Temperatures

Figure 3 shows the deuterium permeation flux–time curves of 310S stainless steel at 733, 786, and 838 K. As the test temperature increased, the steady-state permeation flux increased markedly, while the time required to reach the steady state decreased accordingly, indicating that hydrogen isotope transport in 310S stainless steel exhibited a pronounced thermally activated character. At 838 K, the permeation flux increased rapidly and stabilized within a relatively short period. In contrast, the flux at 733 K remained much lower and showed a longer time lag, suggesting that the migration of hydrogen isotopes in the austenitic matrix was more strongly restricted at lower temperatures.

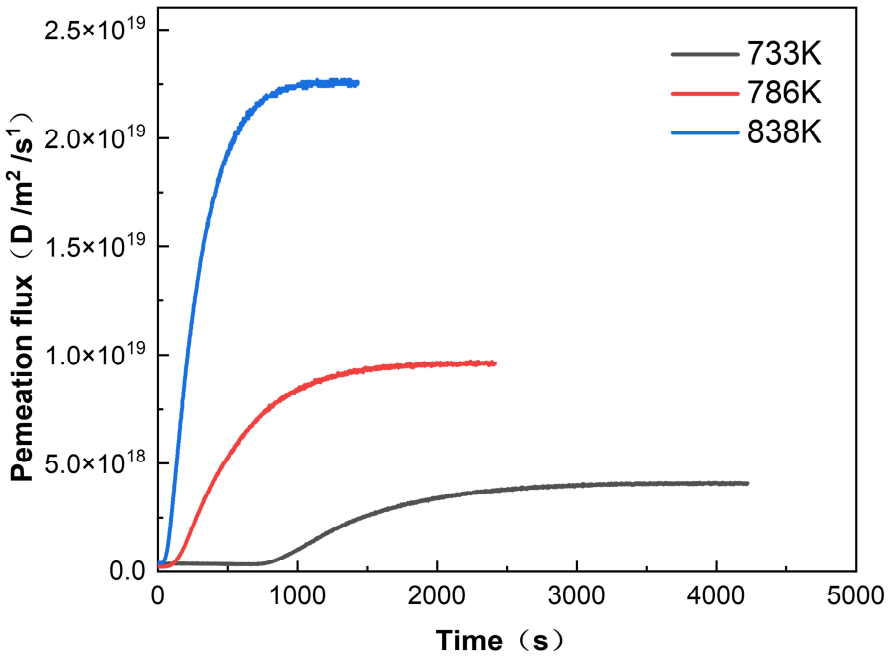

Figure 3. Steady-state deuterium permeation flux curves of 310S steel at different temperatures.

The steady-state permeation flux can be described by the permeability, P. As shown in Figure 4a, the deuterium permeability of 310S stainless steel followed an Arrhenius-type relationship:

$$P = 8.86 \times 10^{-6} exp(-\frac{8.265 \times 10^4}{RT}) \quad (2)$$

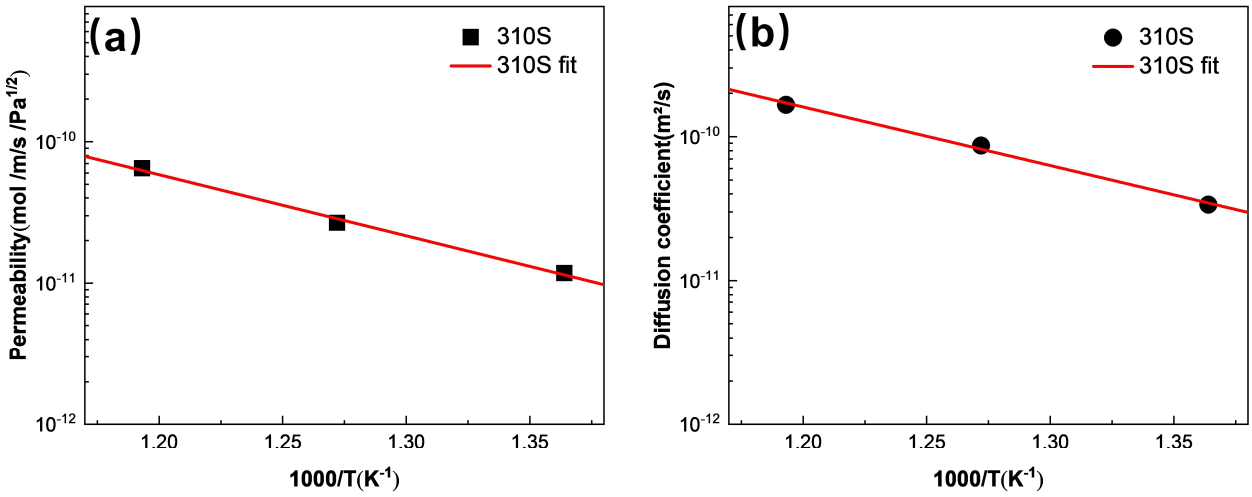

Figure 4. Temperature dependence of deuterium transport parameters in 310S stainless steel: (**a**) deuterium permeability; (**b**) deuterium diffusion coefficient.

The results indicate that, within the investigated temperature range of 733–838 K, the deuterium permeability increased exponentially with temperature, confirming that elevated temperature significantly promoted the coupled dissolution–diffusion transport of hydrogen isotopes in 310S stainless steel. The diffusion coefficient, D, was further determined from the permeation time-lag behavior at different temperatures, as shown in Figure 4b:

$$D = 1.22 \times 10^{-5} exp(-\frac{7.784 \times 10^4}{RT}) \quad (3)$$

At 838 K, the diffusion of hydrogen isotopes in 310S was the fastest, with a diffusion coefficient of 1.66392×10^{-10} m^2/s. When the temperature decreased to 786 K and 733 K, the diffusion coefficients decreased to 8.67757×10^{-11} m^2/s and 3.37461×10^{-11} m^2/s, respectively. By extrapolation, the diffusion coefficient at 673 K was estimated to be approximately 1.11×10^{-11} m^2/s.

These results demonstrate that the hydrogen isotope transport behavior of 310S stainless steel in the present temperature range was predominantly controlled by thermal activation. Owing to the relatively high hydrogen solubility and low diffusion rate of the stable FCC austenitic structure, hydrogen isotopes tend to form a surface-enriched and inwardly delayed concentration profile at lower temperatures. With increasing temperature, however, the ability of hydrogen isotopes to overcome diffusion barriers is enhanced, leading to more efficient transport into the interior of the material, as reflected by the increased permeation flux and shortened time lag. The extrapolated diffusion coefficient at 673 K further suggests that, although hydrogen isotopes can enter the near-surface region within a short time, several hours are still required to establish a nearly uniform concentration distribution across a millimeter-scale specimen. This provides the basis for understanding the distinct charging states obtained at 673 K under different charging durations.

3.2. Hydrogen Isotope Retention Behavior and Two-Dimensional Diffusion Simulation Under Different Charging Times

Figure 5 shows the TDS curves of 310S stainless steel after gaseous deuterium charging at 673 K for 1 min and 4 h. Clear differences were observed in both the peak shape and the peak intensity. This indicates that charging time had a significant effect on hydrogen isotope retention. For the 673 K-1 min-D specimen, the deuterium uptake per unit area was 2187.63×10^{18} $D \cdot m^{-2}$. Only a weak and broad desorption peak appeared in the range of 750–850 K. This result suggests that, after short-time charging, deuterium was mainly retained in the near-surface region and only limited penetration occurred. In contrast, the deuterium uptake of the 673 K-4 h-D specimen increased to $13{,}693.04 \times 10^{18}$ $D \cdot m^{-2}$, which was about 6.26 times that of the 1 min condition. A clear main desorption peak appeared in the range of 800–900 K. This indicates that hydrogen isotopes had diffused further into the specimen and occupied more trapping sites with higher binding energy. Therefore, the 673 K-1 min-D condition can be regarded as a short-time unsaturated charging state, whereas the 673 K-4 h-D condition represents a long-time charging state with much higher retention.

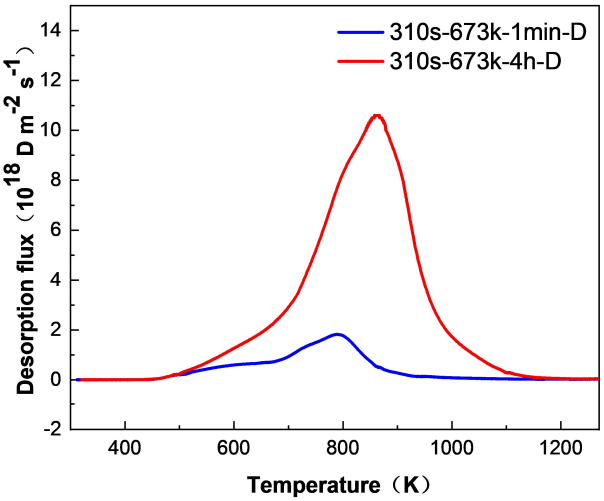

Figure 5. Thermal desorption spectroscopy (TDS) curves of 310S steel after gaseous deuterium charging at 673 K for 1 min and 4 h.

To further evaluate the evolution of hydrogen isotope concentration at 673 K, a two-dimensional diffusion model was established based on Fick's second law. The gauge section of the miniature dog-bone specimen was approximated as a rectangular cross-section with a width of 1.2 mm and a thickness of 1.0 mm. Because the gauge length was much larger than the cross-sectional dimensions, the concentration gradient during the initial and intermediate charging stages was mainly controlled by diffusion along the width and thickness directions. The diffusion of hydrogen isotopes in the specimen can therefore be described by the two-dimensional form of Fick's second law:

$$\frac{\partial C(x,y,t)}{\partial t} = D\left(\frac{\partial^2 C(x,y,t)}{\partial x^2} + \frac{\partial^2 C(x,y,t)}{\partial y^2}\right) \tag{4}$$

The surface deuterium concentration was assumed to remain constant at Cs, the initial concentration in the material was set to zero, and the diffusion coefficient was taken as $D_{673\mathrm{K}} = 1.11 \times 10^{-11}$ m^2/s. The half-width and half-thickness were a = 0.6 mm and b = 0.5 mm, respectively, and x and y represent the width and thickness coordinates of the specimen cross-section. Based on the analytical solution, the normalized average deuterium concentration over the cross-section, $\overline{C}(t)/Cs$, and the normalized deuterium concentration at the specimen center, $\overline{C}(t)/Cs$, were obtained as follows:

$$\frac{\overline{C}(t)}{C_s} = 1 - \left[\frac{8}{\pi^2}\sum_{n=0}^{\infty}\frac{1}{(2n+1)^2}\exp\left(-\frac{(2n+1)^2\pi^2 Dt}{4a^2}\right)\right]\cdot\left[\frac{8}{\pi^2}\sum_{m=0}^{\infty}\frac{1}{(2m+1)^2}\exp\left(-\frac{(2m+1)^2\pi^2 Dt}{4b^2}\right)\right] \tag{5}$$

$$\frac{C_c(t)}{C_s} = 1 - \left[\frac{4}{\pi}\sum_{n=0}^{\infty}\frac{(-1)^n}{2n+1}\exp\left(-\frac{(2n+1)^2\pi^2 Dt}{4a^2}\right)\right]\cdot\left[\frac{4}{\pi}\sum_{m=0}^{\infty}\frac{(-1)^m}{2m+1}\exp\left(-\frac{(2m+1)^2\pi^2 Dt}{4b^2}\right)\right] \tag{6}$$

The simulation results (Figure 6) show that the response of the deuterium concentration at the specimen center lagged behind the overall average concentration, exhibiting a typical evolution feature of surface enrichment followed by inward diffusion. After 1 min charging, the average deuterium concentration was only about 0.10 Cs, while the concentration at the specimen center remained close to zero. After 4 h charging, the average deuterium concentration increased to about 0.955 Cs, and the center concentration reached about 0.888 Cs, indicating that the specimen had approached an overall near-saturated state after long-time high-temperature gaseous charging. Further calculation showed that the average concentration reached 0.95 Cs and 0.99 Cs after about 3.85 h and 6.26 h, respectively, whereas the center concentration required about 5.21 h and 7.61 h to reach the same levels. These results indicate that the charging process was a continuous evolution from surface enrichment to gradual inward diffusion. Extending the charging time increased the overall retained amount of deuterium and enhanced trap occupancy in the specimen interior, thus providing a hydrogen distribution basis for the subsequent differences in mechanical properties and fracture behavior.

3.3. Microstructural Stability Before and After Deuterium Charging

Figure 7a shows the XRD pattern of solution-treated 310S steel. All major diffraction peaks correspond to the FCC austenite phase, indicating that the solution-treated 310S steel had a stable single-phase austenitic structure. As shown in Figure 7b, the microstructure consisted mainly of equiaxed grains with clear grain boundaries. No obvious precipitates were observed, and a small number of annealing twins were present. The microstructure was relatively uniform.

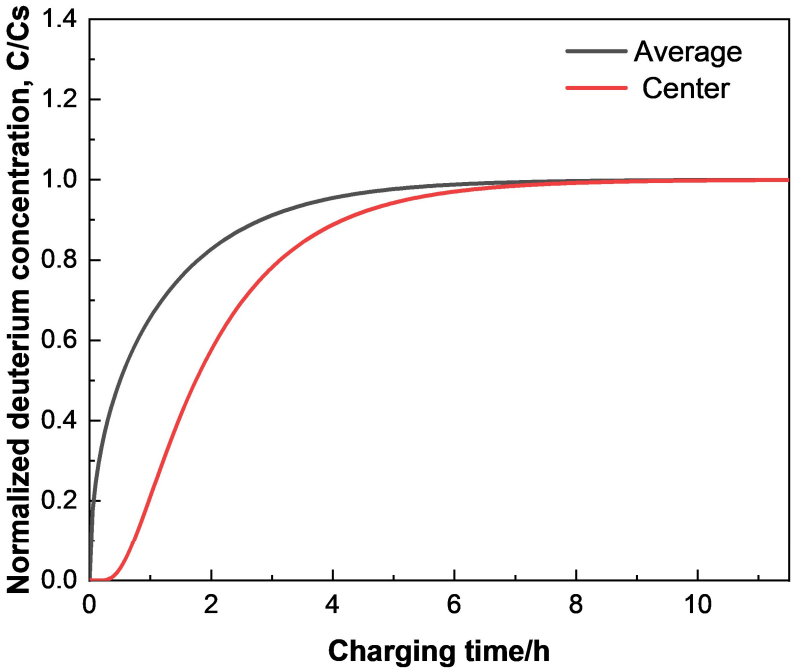

Figure 6. Simulation diagram of deuterium saturation concentration in 310S specimen at 673 K.

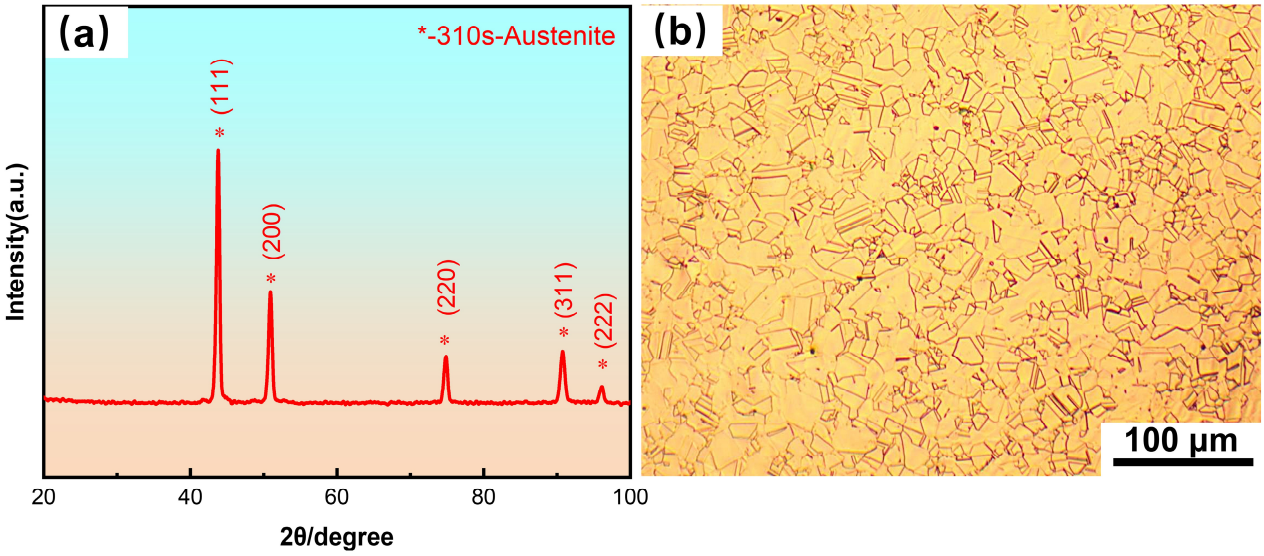

Figure 7. (**a**) X-ray diffraction (XRD) pattern of 310S steel after heat treatment; (**b**) metallographic microstructure of 310S steel.

Figure 8 shows the EBSD inverse pole figure (IPF) maps and phase maps of 310S steel before and after deuterium charging. Before and after charging, the specimens both exhibited a uniform equiaxed grain structure with scattered grain orientations. The microstructure was dominated by γ-austenite, with only a trace amount of ferrite near local grain boundaries. No obvious phase transformation or microstructural instability was induced by deuterium charging.

These results indicate that the role of hydrogen in the present study was mainly related to local diffusion, segregation, and trapping, rather than to a change in phase constitution. Therefore, the differences in mechanical properties and fracture behavior before and after deuterium charging were not caused by microstructural type variation, but were mainly associated with the change in hydrogen isotope distribution within the stable austenitic matrix.

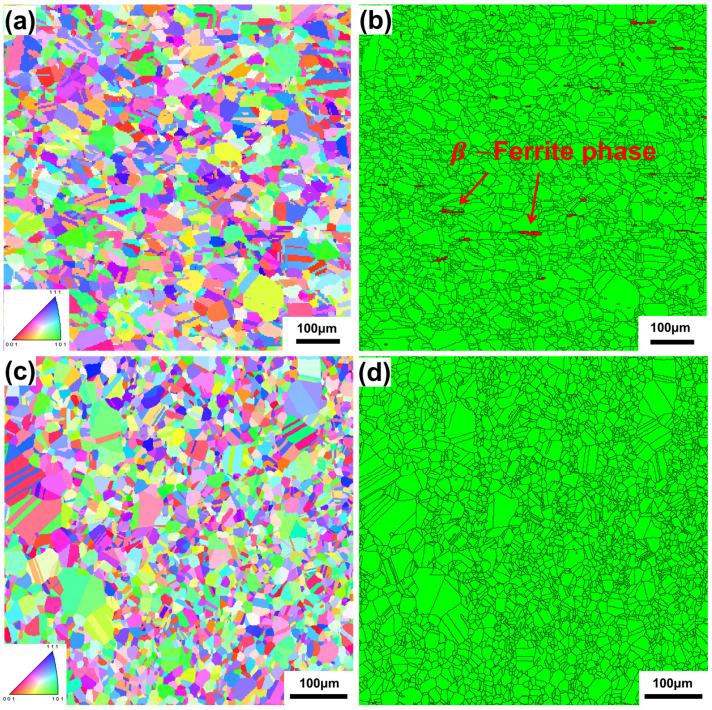

Figure 8. EBSD inverse pole figure (IPF) maps and phase distribution maps of 310S steel before and after deuterium charging; (**a**,**b**) IPF map and phase map before deuterium charging; (**c**,**d**) IPF map and phase map after deuterium charging.

3.4. Mechanical Properties and Fracture Behavior Under Different Charging Conditions

Figure 9 shows the engineering stress–strain curves of 310S steel in the RT, 673 K-1 min-D, and 673 K-4 h-D conditions, and the corresponding mechanical properties are listed in Table 2. All three curves show continuous yielding, indicating that stable austenitic plastic deformation remained dominant under different charging conditions. For the RT specimen, the yield strength, ultimate tensile strength, and elongation were 379.08 MPa, 606.97 MPa, and 46.24%, respectively. After deuterium charging for 1 min, these values were 379.08 MPa, 611.91 MPa, and 46.69%, respectively. After 4 h of deuterium charging, they were 374.25 MPa, 610.84 MPa, and 46.17%, respectively. Overall, the mechanical properties changed only slightly. This indicates that high-temperature gaseous deuterium charging did not cause obvious macroscopic plastic loss under the present room-temperature tensile condition.

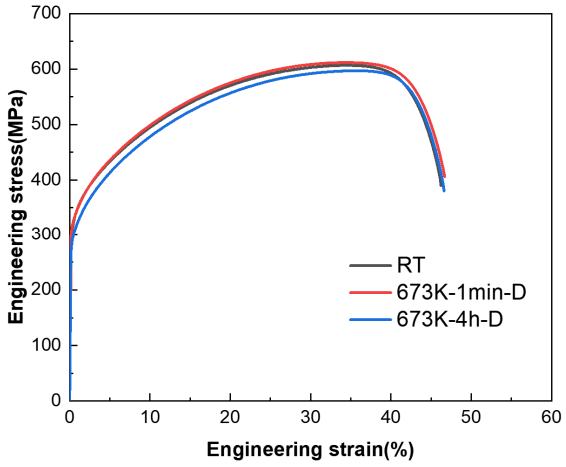

Figure 9. Stress–strain curves of 310S stainless steel under different deuterium-charging conditions.

Table 2. Mechanical properties of 310S stainless steel under different deuterium-charging conditions.

Alloys	YS (MPa)	UTS (MPa)	EL, δ (%)	EL Loss, I_δ (%)
RT	379.08 ± 12.37	606.97 ± 11.95	46.24 ± 1.03	—
673 K-1 min-D	379.08 ± 5.66	611.91 ± 0.17	46.69 ± 1.31	≈0
673 K-4 h-D	374.25 ± 3.84	610.84 ± 0.23	46.17 ± 1.50	≈0

Figure 10 shows the fracture morphologies under different charging conditions. In the RT state, the fracture surface contained abundant dimples, showing typical ductile fracture characteristics. After 1 min of deuterium charging, small secondary cracks and a few relatively flat regions appeared locally on the fracture surface, indicating that deuterium had begun to affect local damage initiation, although its effect was still mainly limited to the surface and edge-sensitive regions. After 4 h of deuterium charging, more smooth facets, tear ridges, and secondary cracks were observed near the fracture center. Local quasi-cleavage-like features also became more obvious. These results suggest that localized hydrogen-assisted fracture features became more evident with increasing charging time, although the overall fracture mode still remained predominantly ductile.

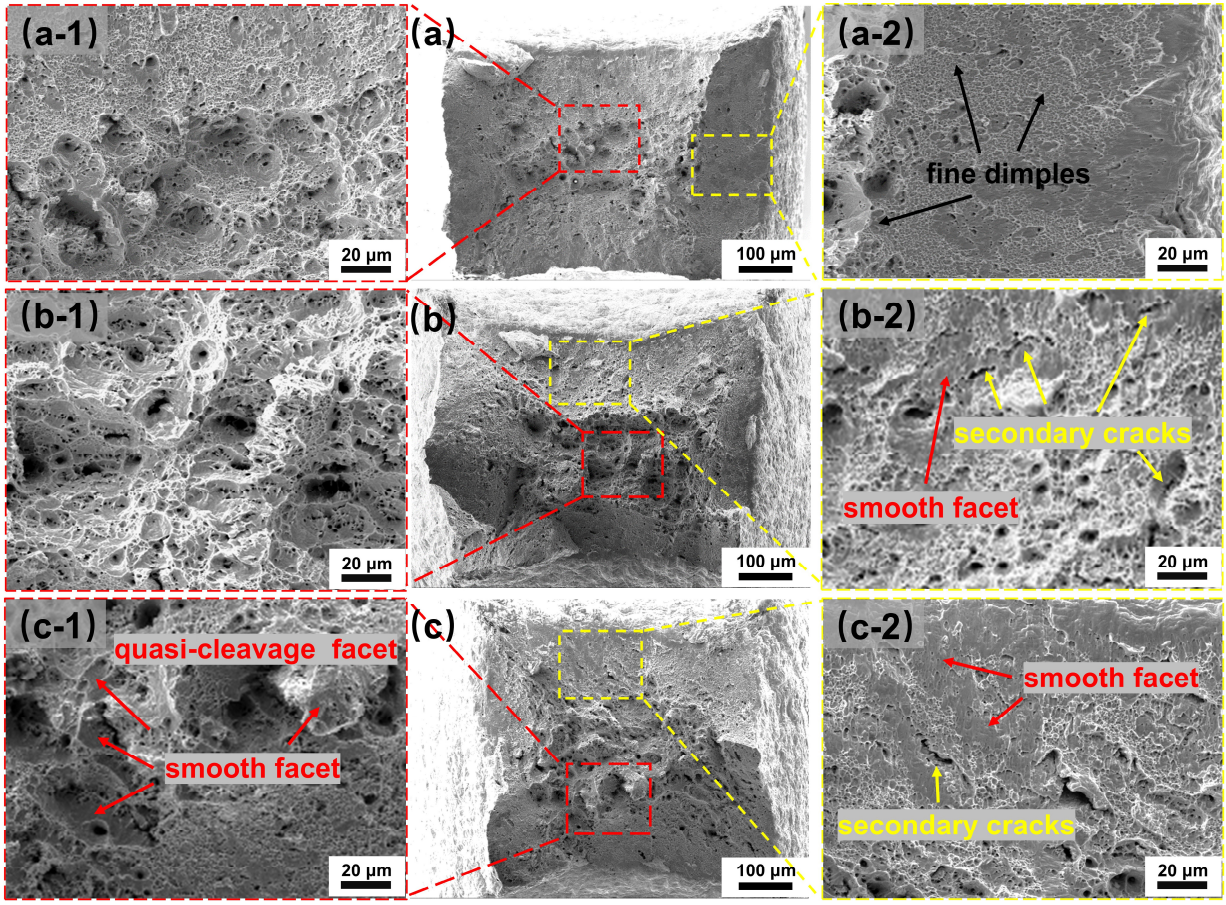

Figure 10. Scanning electron microscope (SEM) images of fracture morphologies of 310S stainless steel specimens under different deuterium-charging conditions: (**a**) an overview micrograph of the room-temperature (RT) specimen; (**a-1**,**a-2**) high-magnification images of the fracture areas marked in (**a**); (**b**) overview micrograph of the specimen after deuterium charging at 673 K for 1 min; (**b-1**,**b-2**) high-magnification images of the fracture areas marked in (**b**); (**c**) an overview micrograph of the specimen after deuterium charging at 673 K for 4 h; (**c-1**,**c-2**) high-magnification images of the fracture areas marked in (**c**).

Combined with the TDS results and the two-dimensional diffusion simulation, the fracture observations indicate that high-temperature gaseous deuterium charging increased the retained hydrogen isotope content and changed its distribution from a surface-enriched state to deeper inward diffusion and trapping. Although the 673 K-4 h-D specimen exhibited a much higher deuterium retention level than the 673 K-1 min-D specimen, the tensile properties changed only slightly. This indicates that the macroscopic mechanical response of 310S stainless steel was not simply proportional to the total retained deuterium amount, and that local hydrogen isotope distribution should be considered when interpreting the fracture behavior.

This difference between macroscopic tensile properties and local fracture features can be understood from the different length scales involved in tensile deformation and fracture initiation. The engineering stress–strain response reflects the overall load-bearing and plastic deformation capacity of the specimen, whereas fracture morphology is more sensitive to local hydrogen enrichment, defect distribution, and stress concentration near crack initiation and propagation sites. As confirmed by XRD and EBSD, no obvious hydrogen-induced phase transformation occurred after deuterium charging. Therefore, the high austenite stability and retained plastic deformation capability of the FCC matrix helped maintain the macroscopic tensile properties under the present room-temperature tensile condition [9,10].

Nevertheless, deuterium atoms could still accumulate in near-surface regions, grain boundaries, dislocation structures, and other defect-sensitive sites. These locally enriched regions may promote microcrack initiation and local crack propagation through hydrogen-enhanced localized plasticity, reduced local cohesive strength, and defect-assisted damage evolution [12–16]. As a result, secondary cracks, smooth facets, serrated edges, and local quasi-cleavage-like features became more evident after deuterium charging, especially in the 673 K-4 h-D condition. However, these localized features did not develop into a dominant brittle fracture mode, and abundant ductile dimples were still observed. Therefore, the fracture mode after deuterium charging can be described as predominantly ductile fracture with enhanced local hydrogen-assisted damage.

These results suggest that the embrittlement response of 310S stainless steel under high-temperature gaseous deuterium charging is governed not only by the total retained hydrogen isotope amount, but also by the spatial distribution of hydrogen isotopes, local defect structures, and stress state at critical load-bearing regions. Increased deuterium retention after long-time charging mainly intensified local hydrogen-assisted fracture features, while the stable austenitic matrix still maintained the overall tensile plasticity. Similar dual effects of hydrogen on local damage evolution and plastic deformation in stable Fe–Cr–Ni austenitic steels have also been reported in previous studies [34–39]. Further investigations with more charging durations and different strain rates would help establish a more quantitative relationship among retained amount, local hydrogen distribution, and macroscopic mechanical response.

4. Conclusions

1. The hydrogen isotope permeability and diffusion coefficient of 310S austenitic stainless steel increased significantly with increasing temperature and followed an Arrhenius relationship. The diffusion coefficient extrapolated at 673 K was about 1.11×10^{-11} m^2/s, indicating that several hours were still required to establish a nearly uniform hydrogen isotope distribution across a millimeter-scale specimen.
2. At 673 K, the hydrogen isotope retention behavior was strongly affected by charging time. Combined TDS and two-dimensional Fick diffusion simulation showed that 673 K-1 min-D corresponded to a typical unsaturated surface-enriched state, whereas

673 K-4 h-D represented an overall near-saturated high-retention state, although the specimen center still remained slightly below the surface equilibrium concentration.

3. High-temperature gaseous deuterium charging had little effect on the yield strength and ultimate tensile strength of 310S stainless steel, but it changed the local fracture characteristics. Secondary cracks, serrated edges, and local quasi-cleavage-like features became more evident after charging, especially in the 4 h condition, indicating that hydrogen isotopes participated in local damage initiation and crack propagation.
4. XRD, metallography, and EBSD results confirmed that 310S stainless steel maintained good austenitic stability under the present charging conditions, and no obvious hydrogen-induced phase transformation was observed. The embrittlement response of 310S was therefore not directly determined by the total retained amount alone, but was more closely related to the local distribution of hydrogen isotopes in the surface region, defect-rich areas, and key load-bearing zones.

Author Contributions: Conceptualization, Z.H.; methodology, Y.J. and Z.H.; formal analysis, Y.J. and Z.W.; investigation, Y.J. and Z.W.; writing—original draft preparation, Y.J.; writing—review and editing, Z.H.; visualization, Y.J.; supervision, Z.H.; funding acquisition, J.L. All authors have read and agreed to the published version of the manuscript.

Funding: This research was funded by International Science and Technology Cooperation Project of Qinghai Provincial Department of Science and Technology, grant number 2024-HZ-807.

Data Availability Statement: The original contributions presented in this study are included in the article. Further inquiries can be directed to the corresponding author.

Acknowledgments: The authors appreciate the assistance provided by the Institute of Plasma Physics, Chinese Academy of Sciences for high-temperature gaseous deuterium charging.

Conflicts of Interest: The authors declare no conflict of interest.

References

1. Liu, J.; Zhao, M.; Rong, L. Overview of hydrogen-resistant alloys for high-pressure hydrogen environment: On the hydrogen energy structural materials. *Clean Energy* **2023**, *7*, 99–115. [CrossRef]
2. Yu, H.; Díaz, A.; Lu, X.; Sun, B.; Ding, Y.; Koyama, M.; He, J.; Zhou, X.; Oudriss, A.; Feaugas, X.; et al. Hydrogen embrittlement as a conspicuous material challenge—Comprehensive review and future directions. *Chem. Rev.* **2024**, *124*, 6271–6392. [CrossRef]
3. Gao, M.; Cheng, Z.; Dong, L.; Wang, S.; Huang, Y.; Mao, X. Effect of V–Ti multi-microalloying on enhancing hydrogen embrittlement resistance in hot-stamping steel. *J. Mater. Res. Technol.* **2024**, *33*, 6990–7003. [CrossRef]
4. Huang, C.; Cai, W.; Qi, L.; Wang, Z.; Guan, R. Role of rare-earth yttrium in the hydrogen embrittlement of AISI 321 austenitic stainless steel. *Int. J. Hydrogen Energy* **2022**, *47*, 37138–37152. [CrossRef]
5. Omura, T.; Oyama, T. Effects of the addition of alloying elements on hydrogen diffusion and hydrogen embrittlement in martensitic steel. *ISIJ Int.* **2024**, *64*, 620–629. [CrossRef]
6. Pu, S.D.; Turk, A.; Lenka, S.; Ooi, S.W. Study of hydrogen release resulting from the transformation of austenite into martensite. *Mater. Sci. Eng. A* **2019**, *754*, 628–635. [CrossRef]
7. Reda, R.; Ataya, S.; Ayman, M.; Saad, K.; Mostafa, S.; Elnady, G.; Khan, R.; Elshaghoul, Y.G.Y. Additively manufactured 316L stainless steel: Hydrogen embrittlement susceptibility and electrochemical gas production. *Appl. Sci.* **2025**, *15*, 5824. [CrossRef]
8. Luo, Y.; Li, W.; Jiang, L.; Zhong, N.; Jin, X. Hydrogen embrittlement and hydrogen diffusion behavior in interstitial nitrogen-alloyed austenitic steel. *Int. J. Hydrogen Energy* **2021**, *46*, 32710–32722. [CrossRef]
9. Hwang, B.-K.; Kim, H.-T.; Cha, S.-J.; Park, G.-S.; Yoon, J.-T.; Kim, J.-H.; Lee, J.-M. Comparative study of hydrogen embrittlement in 310S, 304L, and 316L stainless steels under in situ electrochemical hydrogen charging. Part 1: Experimental study. *Eng. Fail. Anal.* **2025**, *176*, 109641. [CrossRef]
10. Li, W.; Wu, W.; Yang, Z.; Liu, M.; Li, S.; Li, J. Enhancement of hydrogen embrittlement resistance in 310S austenitic stainless steel through ribbon-like δ-ferrite. *Corros. Sci.* **2024**, *233*, 112086. [CrossRef]
11. Barrera, O.; Bombac, D.; Chen, Y.; Daff, T.D.; Galindo-Nava, E. Understanding and mitigating hydrogen embrittlement of steels: A review of experimental, modelling and design progress from atomistic to continuum. *J. Mater. Sci.* **2018**, *53*, 6251–6290. [CrossRef] [PubMed]

12. López Freixes, M.; Zhou, X.; Zhao, H.; Godin, H.; Peguet, L.; Warner, T.; Gault, B. Revisiting stress-corrosion cracking and hydrogen embrittlement in 7xxx-Al alloys at the near-atomic-scale. *Nat. Commun.* **2022**, *13*, 4290. [CrossRef]
13. Fagnoni, F.; Kursun, E.C.; Busi, M.; Konarski, P.; Yetik, O.; Spolenak, R.; Bertsch, J.; Duarte, L.I. Hydrogen enhanced localized plasticity in zirconium as observed by digital image correlation. *J. Nucl. Mater.* **2024**, *590*, 154873. [CrossRef]
14. Song, J.; Curtin, W.A. A nanoscale mechanism of hydrogen embrittlement in metals. *Acta Mater.* **2011**, *59*, 1557–1569. [CrossRef]
15. Liang, S.; Huang, M.; Zhao, L.; Zhu, Y.; Li, Z. Effect of multiple hydrogen embrittlement mechanisms on crack propagation behavior of FCC metals: Competition vs. synergy. *Int. J. Plast.* **2021**, *143*, 103023. [CrossRef]
16. Guzmán, A.A.; Janisch, R. Effects of mechanical stress, chemical potential, and coverage on hydrogen solubility during hydrogen-enhanced decohesion of ferritic steel grain boundaries: A first-principles study. *Phys. Rev. Mater.* **2024**, *8*, 073601. [CrossRef]
17. Falat, L.; Čiripová, L.; Petruš, O.; Puchý, V.; Petryshynets, I.; Kovaľ, K.; Džunda, R. The effects of electrochemical hydrogen charging on Charpy impact toughness and dry sliding tribological behavior of AISI 316H stainless steel. *Crystals* **2023**, *13*, 1249. [CrossRef]
18. Weihrauch, M.; Patel, M.; Patterson, E.A. Measurements and predictions of diffusible hydrogen escape and absorption in catholically charged 316LN austenitic stainless steel. *Sci. Rep.* **2023**, *13*, 10545. [CrossRef]
19. Todoshchenko, O.; Yagodzinskyy, Y.; Papula, S.; Hänninen, H. Hydrogen solubility and diffusion in metastable austenitic stainless steels studied with thermal desorption spectroscopy. In *International Hydrogen Conference (IHC 2012): Hydrogen-Materials Interactions*; Somerday, B.P., Sofronis, P., Eds.; ASME Press: New York, NY, USA, 2014; pp. 615–623.
20. Duportal, M.; Oudriss, A.; Feaugas, X.; Savall, C. On the estimation of the diffusion coefficient and distribution of hydrogen in stainless steel. *Scr. Mater.* **2020**, *186*, 282–286. [CrossRef]
21. Eichinger, M.; Pengg, J.; Zwittnig, D.; Mori, G. Hydrogen diffusivity, uptake and embrittlement of solution annealed and cold deformed austenitic stainless steel 1.4435 at hydrogen pressures up to 1000 bar and 200 °C. *Corros. Sci.* **2024**, *235*, 112219. [CrossRef]
22. Hempel, C.; Mandel, M.; Quitzke, C.; Wendler, M.; Kreschel, T.; Volkova, O.; Krüger, L. Hydrogen diffusion in deformed austenitic TRIP steel—A study of mathematical prediction and experimental validation. *Materials* **2024**, *17*, 6114. [CrossRef]
23. Hu, Q.; Cheng, Y.F. Effect of electrochemical hydrogen-charging conditions on nanomechanical properties of X80 pipeline steel. *Eng. Fail. Anal.* **2024**, *160*, 108242. [CrossRef]
24. Rahimi, S.; Verbeken, K.; Depover, T.; Proverbio, E. Hydrogen embrittlement of pipeline steels under gaseous and electrochemical charging: A comparative review on tensile properties. *Eng. Fail. Anal.* **2025**, *167*, 108956. [CrossRef]
25. Shen, X.; Xu, Y.-P.; Zhang, S.-B.; Wen, P.-Y.; Zhou, H.-S.; Chen, H.; Liu, W.; Luo, G.-N. Hydrogen isotope permeation and retention behavior in the RAFM steel manufactured by laser powder bed fusion. *J. Nucl. Mater.* **2024**, *596*, 155092. [CrossRef]
26. Hu, X.; Lach, T.G.; Terrani, K.A. Deuterium permeation and retention in 316L stainless steel manufactured by laser powder bed fusion. *J. Nucl. Mater.* **2021**, *548*, 152871. [CrossRef]
27. Chen, Z.; Hu, X.; Ye, M.; Wirth, B.D. Deuterium transport and retention properties of representative fusion blanket structural materials. *J. Nucl. Mater.* **2021**, *549*, 152904. [CrossRef]
28. San Marchi, C.; Somerday, B.P.; Robinson, S.L. Permeability, solubility and diffusivity of hydrogen isotopes in stainless steels at high gas pressures. *Int. J. Hydrogen Energy* **2007**, *32*, 100–116. [CrossRef]
29. Liu, F.; Zhou, H.S.; Li, X.C.; Xu, Y.P.; An, Z.Q.; Mao, H.; Xing, W.; Hou, Q.; Luo, G.N. Deuterium gas-driven permeation and subsequent retention in rolled tungsten foils. *J. Nucl. Mater.* **2014**, *455*, 248–252. [CrossRef]
30. Zhou, H.S.; Liu, H.D.; An, Z.Q.; Li, B.; Xu, Y.P.; Liu, F.; Zhao, M.Z.; Xu, Q.; Ding, F.; Luo, G.N. Deuterium permeation and retention in copper alloys. *J. Nucl. Mater.* **2017**, *493*, 398–403. [CrossRef]
31. Tao, Z.H.; Liu, H.D.; Zhao, S.X.; Li, X.C.; Liu, C.B.; Zhu, Y.W.; Wang, C.; Zhou, H.S.; Luo, G.N. Deuterium permeation and retention behavior in copper-based brazing filler materials. *Nucl. Mater. Energy* **2024**, *40*, 101694. [CrossRef]
32. Jiang, Y.-B.; Jiang, W.; Si, N.; Wang, Z. Hydrogen storage properties of MgH_2 + Mg_2NiH_4–Co/C ternary nanocomposite. *Int. J. Hydrogen Energy* **2024**, *72*, 258–267. [CrossRef]
33. Felderhoff, M.; Bogdanović, B. High temperature metal hydrides as heat storage materials for solar and related applications. *Int. J. Mol. Sci.* **2009**, *10*, 325–344. [CrossRef] [PubMed]
34. Ogawa, Y.; Hosoi, H.; Tsuzaki, K.; Redarce, T.; Takakuwa, O.; Matsunaga, H. Hydrogen, as an alloying element, enables a greater strength-ductility balance in an Fe-Cr-Ni-based, stable austenitic stainless steel. *Acta Mater.* **2020**, *199*, 181–192. [CrossRef]
35. Ogawa, Y.; Nishida, H.; Takakuwa, O.; Tsuzaki, K. Hydrogen-enhanced deformation twinning in Fe-Cr-Ni-based austenitic steel characterized by in-situ EBSD observation. *Mater. Today Commun.* **2023**, *34*, 105433. [CrossRef]
36. Ogawa, Y.; Tanaka, M.; Fujita, T.; Shibata, A. Thermally activated dislocation motion in hydrogen-alloyed Fe–Cr–Ni austenitic steel revisited via Haasen plot. *Int. J. Hydrogen Energy* **2024**, *74*, 170–182. [CrossRef]
37. Ogawa, Y.; Takakuwa, O.; Tsuzaki, K. Solid-solution hardening by hydrogen in Fe–Cr–Ni-based austenitic steel: Temperature and strain rate effects. *Mater. Sci. Eng. A* **2023**, *879*, 145281. [CrossRef]

38. Ogawa, Y.; Shibata, A. Refining hydrogen-dislocation interaction model for thermally activated plasticity in Fe-Cr-Ni austenitic steels: Analyzing stress-dependent activation volume. *Acta Mater.* **2026**, *306*, 121896. [CrossRef]
39. Nishida, H.; Ogawa, Y.; Tsuzaki, K. Chemical composition dependence of the strength and ductility enhancement by solute hydrogen in Fe–Cr–Ni-based austenitic alloys. *Mater. Sci. Eng. A* **2022**, *836*, 142681. [CrossRef]